

# Characterization of Temperature Fields in Laser Beam Welded Hollow-Cylindrical Cold Crack Samples from High Strength Steel 100Cr6

Eric Wasilewski (✉ [eric.wasilewski@b-tu.de](mailto:eric.wasilewski@b-tu.de))

Brandenburg University of Technology Cottbus - Senftenberg <https://orcid.org/0000-0002-2637-5586>

Nikolay Doynov

Brandenburg University of Technology Cottbus - Senftenberg

Ralf Ossenbrink

Brandenburg University of Technology Cottbus - Senftenberg

Vesselin Michailov

Brandenburg University of Technology Cottbus - Senftenberg

---

## Research Article

**Keywords:** Computational welding mechanics, Finite element simulation, Laser beam welding, Heat transfer, Temperature rate, Phase transformation

**Posted Date:** December 20th, 2021

**DOI:** <https://doi.org/10.21203/rs.3.rs-1149427/v1>

**License:**  This work is licensed under a Creative Commons Attribution 4.0 International License.

[Read Full License](#)

---

# Characterization of temperature fields in laser beam welded hollow-cylindrical cold crack samples from high strength steel 100Cr6

## Authors (ORCID)

Eric Wasilewski (0000-0002-2637-5586); E-Mail: eric.wasilewski@b-tu.de,

Nikolay Doynov (0000-0002-3462-0190),

Ralf Ossenbrink,

Vesselin Michailov (0000-0002-7886-3637)

Department of Joining and Welding Technology

Brandenburg University of Technology Cottbus - Senftenberg

03046 Cottbus, Germany

## Abstract

This work presents a comparative study of thermal conditions that occur during laser beam welding of high strength steel 100Cr6 that often leads to a loss of technological strength and may conditionally produce cold cracks. The results from both experiments and thermal-metallurgical FE-simulations indicate that the type of heat coupling changes significantly when welding with different process parameters, e.g., in the transition between conduction and deep penetration welding. Further, the simulations show that as a result of the high welding speeds and reduced energy per unit length, extremely high heating rates of up to  $2 \times 10^4 \text{ K s}^{-1}$  (set A) resp.  $4 \times 10^5 \text{ K s}^{-1}$  (set B) occur in the material. Both welds thus concern a range of values for which conventional Time-Temperature-Austenitization (TTA) diagrams are not currently defined, so that the material models can only be calibrated using general assumptions. This noted change in energy per unit length and welding speeds causes significantly steep temperature gradients with a slope of approximately  $5 \times 10^3 \text{ K mm}^{-1}$  and strong drops in the heating and cooling rates, particularly in the heat affected zone near the weld metal. This means that even short distances along the length present a staggering difference in relation to the temperature peaks. The temperature cycles also show very different cooling rates for the respective parameter sets, although in both cases they are well below a cooling time  $t_{8/5}$  of one second, so that the phase transformation always leads to the formation of martensite. The results from this study are intended to be used for further detailed experimental and numerical investigation of microstructure, hydrogen distribution, and stress-strain development at different restrain conditions.

## Keywords

Computational welding mechanics, Finite element simulation, Laser beam welding, Heat transfer, Temperature rate, Phase transformation

## 1. Introduction

Process and manufacturing technologies, and welding in particular, must keep up with the development of base materials in respect to weldability. Among welding technologies, laser beam welding specifically plays an important role for a variety of high-strength steel applications. Although there are a number of designs of cold crack testing, the application to hollow cylinders or small tubes is still a critical issue. In addition to the geometric peculiarities, the welding conditions are often considerably different. Complex phenomena, such as solidification, microstructural transformation, defects formation, and hydrogen diffusion have a significant influence on the quality of welded joints and especially on cold crack susceptibility [1] temporally. Numerical simulations can contribute significantly to analyze and better understand the influences of welding processes. With this in mind, the primary goal in this analysis is the realistic consideration of temperature fields, as all discussed problems and phenomena depend on its impacts and ramifications.

The cold cracking phenomenon is not limited to the characteristics of the cooling phase only, but to the entire thermal history as far as it influences the microstructure and hydrogen diffusion and thus the mechanical behavior during welding. While the heat distribution depends largely on the material properties and the initial and boundary conditions, in practical applications the formulation of heat conduction problems even with an appropriate heat source model is well-established. In the literature, different heat sources are discussed. Typically, sources with a function-analytical power distribution on a line, an area, or within a volume are used. According to Radaj [2], further model simplifications relate to the spatial movement of the source relative to the work piece and the sequential order of different heat sources. The most common formulation of heat input, which is also suitable for complex welds, is given by area and volume-distributed sources that can be super-positioned in a suitable manner. According to Radaj and Rykalin [3, 4], surface as well as cylindrical-shaped volume sources with a Gaussian normal distribution have been proven. Goldak [5] also describes a cone-shaped, radial normally distributed heat source with linearly increasing heat output over the depth for deep welding processes. Recent studies describe the adaptation of these sources to map complex welding tasks, such as multi-physical [6] or multi-material [7] laser beam welding problems. These recent models deepen the investigations of Xu [8], who proposes a comparable source type with parabolic and linear power distribution functions, so that the heat source function depends on radial varying parameters and which uses an increased calibration effort. Chukkan [9] shows a comparison of heat sources and their combinations using the example of laser butt welding of AISI 316L stainless steel sheets. Others such as Sun [10] combine ellipsoidal and conical heat sources, for example. Sun describes the suitability of this model for the transient heat transfer for a controlled pulse key punching process in plasma welding.

The coupling of temperature field calculations and transformation kinetics enables the simulation of the phase distribution and the occurring changes in the material properties. In general (weak coupling), this is realized by transferring the discrete temperature and the temperature gradient or the temperature cycle (temperature profile). The strong coupling relates to the latent heat absorbed or released over transformation, which can be considered to increase calculation accuracy.

High strength steels, such as 100Cr6, which is discussed in this study, undergo a phase transformation to austenite during the heating process, which decomposes to martensite during cooling. Since austenite formation is a non-isothermal, diffusion-controlled  $\alpha \rightarrow \gamma$  transformation process, numerous laser beam welding applications are described in the literature that use the Leblond- Devaux [10] equation to

calculate the transformation behavior during heating. The martensite formation, however, is a diffusion-free  $\gamma \rightarrow \alpha$  transformation process. Here, too, the literature suggests an established model according to Koistinen- Marburger [11]. Using the example of hybrid laser arc welding of AH36 steel in a butt joint configuration, Zhang [12] shows the suitability of these models for common applications. He describes a coupled thermo-mechanical analysis, which performs a calculation of phase transformations to consider phase-dependent mechanical properties as well as the thermal expansion coefficient in the different areas of the heat-affected zone (HAZ). Laser beam welding can cause high power densities on the order of  $10^4$ - $10^5$  W mm<sup>2</sup> which requires great welding velocities of several meters per minute. For this reason, the heating and cooling rates are also very fast [9, 13]. Because of this, the transformation effects require special attention.

The aim of this work is to investigate the temperature field of a high strength steel, 100Cr6, during laser beam welding and characterize the temperature history in different sub-zones of the HAZ. This is done to gather valid and systematic knowledge about the thermal conditions in samples with certain cold crack susceptibility. To accomplish this, a numerical model is developed and applied. The application is realized on a commonly used commercial FE-software, Sysweld, which includes the above-mentioned transformation models.

The first section presents the experimental procedure concerning two application examples. The second section deals with the thermal and metallurgical aspects of the modeling approach. The third section puts the results into a discussion and considers the differences in both examples.

## 2. Experimental Procedure

Welding experiments were conducted using micrographs of the welded joints and measurements of the local temperature cycles. This served to gain validation data. The experiments are carried out on hollow-cylindrical samples with an outer diameter of  $8 \pm 0.02$  mm, an inner diameter of  $4 \pm 0.015$  mm, and a length of  $60 \pm 0.05$  mm. For these experiments, a bainitic high strength steel (100Cr6) was used. The prepared samples were butt-welded in an LS108P laser machine by SITEC Industrietechnologie GmbH (Chemnitz, Germany). A TruDisk 5000 disk laser and a CFO D70 focus optic by TRUMPF GmbH + Co. KG (Ditzingen, Germany) were used to weld with a 100  $\mu$ m focus diameter without filler material and shielding gas. Two sets of welding parameters were defined. The parameters of laser power and welding speed (Table 1) were experimentally determined in previous work [14].

**Table 1: Welding parameters for different parameter sets A and B**

Parameter Set	Laser Power in W	Welding Speed in m/min
A	700	6
B	300	1

The samples were clamped on both sides of the seam (Fig.1) using clamping sleeves placed 10 mm from the center of the seam. The type W25 d8 collet made contact over an area of 502.7 mm<sup>2</sup> and was released after 60 seconds of welding time for each test. The welding angle  $\omega$  was set to 360°. The temperature measurements during welding were performed by means of K-type thermocouples with a single wire diameter of 0.1 mm. The signal was processed through an HBM QuantumX amplifier at 200 Hz.

Considering the high-temperature gradients near the weld pool, the distances from the welding line to the thermocouples were controlled by means of light microscopy before and after welding. The start of the weld seam was aligned in relation to the attached thermocouples at a rotation angle of  $180^\circ$  using the high-precision axis control according to Figure 1.

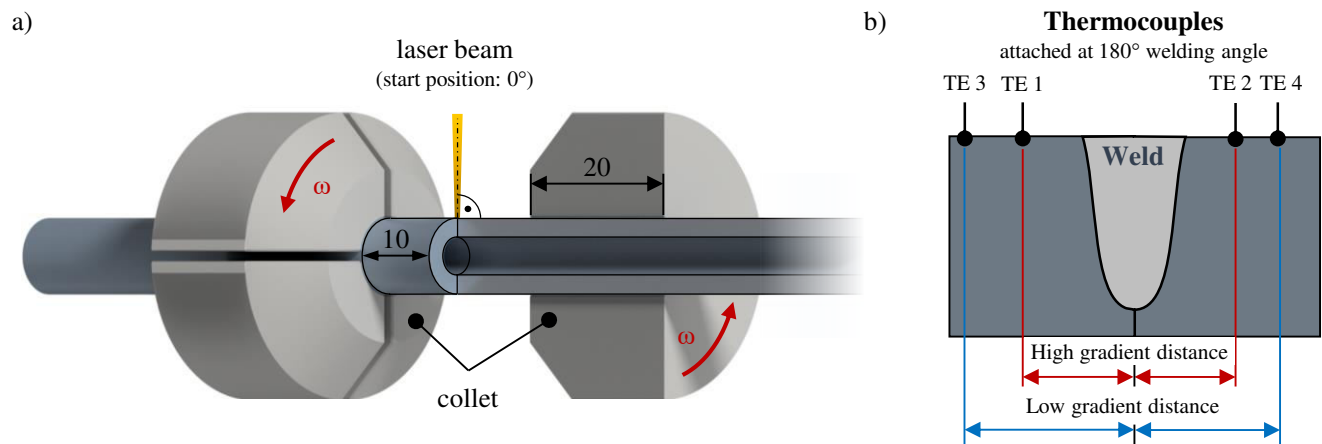


**Figure 1: Experimental setup: (a) Overview and (b) Cross section at  $180^\circ$  welding angle with thermocouple positions**

### 3. Model approach and implementation

#### 3.1 Geometry Model

The FE-model was created to represent transient heat conduction with a moving heat source. For this purpose, axial-symmetric hollow cylinders with a wall thickness of 2 mm, an outer diameter of 8 mm, and a total length of 60 mm were generated, representing a three-dimensional semi-model. The element edge length within the expected weld and heat-affected zone was set to approximately 0.125 mm, so that the mesh was refined only in the area of the large temperature gradient.

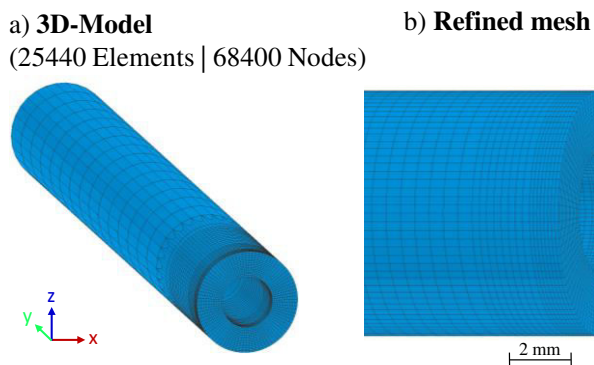


**Figure 2: Finite element mesh, consisting of a combination of 2D elements (left) and 3D elements (right)**

Figure 2 shows the three-dimensional model and its mesh that combines 2D and 3D linear elements. The 2D elements are used here to apply the surface heat source and enable heat transfer conditions to simulate the boundary conditions between the structure and the environment. The 3D elements ensure heat transfer through the basic body structure and enables the definition of a volume acting heat source. Both sub-models are linked using shared nodes. The modeling is also carried out three-dimensionally to investigate the change in the temperature field and the phase distribution over the welding angle. Furthermore, any influence of the reheating at the start of seam can be considered with this approach.

#### 3.2 Heat Source Model

The space and time distribution of the heat introduction through the laser welding process was realized by surface and volume heat source models, super positioned and moving along the weld path synchronously. The heat flow density  $q$  is described by the subsequent equations for the rotating coordinate system  $K'$  of the two heat sources:

1. Surface heat source:

$$q_s(x', y') = \frac{q_0 \cdot \eta_s}{r_0^2 \cdot \pi} \cdot \exp\left(-\frac{x'^2 + y'^2}{r_0^2}\right), \quad (1)$$

2. Volume heat source:

$$q_v(x', y', z') = \frac{1}{h} \cdot \frac{q_0 \cdot \eta_v}{r_0(z')^2 \cdot \pi} \cdot \exp\left(-\frac{x'^2 + y'^2}{r_0(z')^2}\right). \quad (2)$$

The density of the heat flux  $q_s$  (heat flow per unit of surface) and the heat generation rate  $q_v$  (heat flow per unit of volume) at a certain coordinate  $(x', y', z')$  is defined by laser power efficiency coefficients  $\eta_s$  and  $\eta_v$ , respectively, and the Gaussian normal distribution over the radius  $r_0$ . On the surface, the Gaussian distribution only refers to the radial distance from the center of the weld, i.e., projected on the curved surface. In contrast, the radius  $r_0(z')$  of the volume acting Gaussian heat flow distribution depends on the cone height  $h$  ( $z$ -coordinate) and is thus described by the following equation:

$$r_0(z') = r_a + \frac{r_a - r_b}{z_a - z_b} \cdot (z - z_a) \quad (3)$$

where  $r_a$  represents the conical radius on the surface, i.e. at the height of the  $z'$ -coordinate  $z_a$ , and  $r_b$  represents the conical radius at the bottom of the cone, that is, at the level of the  $z'$ -coordinate  $z_b$  in the volume.

Due to the superposition of the surface and volume source, expressing them as a sum of the heat flow rates, the value of the total efficiency  $\eta_{tot}$  must be considered, as the following applies:

$$\eta_{tot} = \frac{1}{q_0} \left( \eta_s \int_S q_s dS + \eta_v \int_V q_v dV \right) \quad \text{with } \eta_{tot} \leq 100\% \quad (4)$$

A sketch of these superpositioned sources is provided in Figure 3.

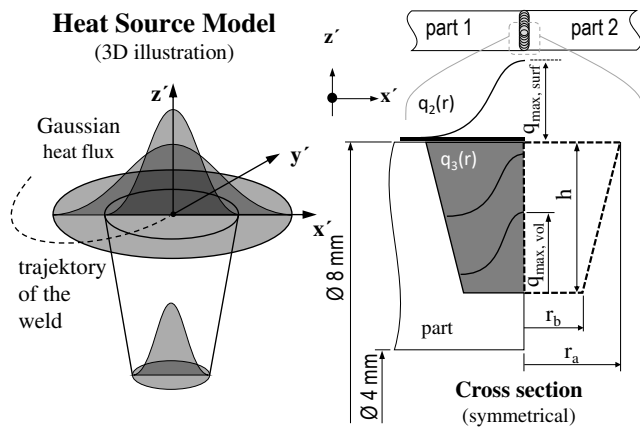


**Figure 3: Graphic representation of the combined heat source model**

In this application, the weld trajectory corresponds to a circular movement on the  $x'$ - $z'$  plane in space, while the coordinates of the rotation axis  $y$  remain unchanged. The  $z'$ -coordinate of the heat source coordinate system is always perpendicular to the cylindrical sample surface. This movement is modeled by coordinate transformation of the cartesian system into the polar coordinate system, so that the transient and two-dimensional movement depends on the angular velocity and the radius of the trajectory, which corresponds to half the outer diameter of the samples. The heat source parameters were determined/calibrated using the welding experimental data. For this purpose, they are adjusted in variation calculations until the real weld seam cross section, and the measured peak temperature distribution and temperature cycles correlate with the simulation result (discussed in Chapter 4).

In addition to the numerical solution, the heating process was calculated analytically to verify heating phase. This was calculated according to the following equation (Eq. 5), which represents a superposition of point-shaped sources along the weld seam depth:

$$T(t, y, z) - T_0 = \frac{1}{n_q} \frac{q_0 \eta_{tot}}{4\pi \lambda} \cdot \exp\left(-\frac{v \cdot (x_0 - v \cdot t)}{2a}\right) \cdot \sum_{j=-1,1} \sum_{n=-\infty}^{\infty} \sum_{k=1}^{n_q} \left(\frac{1}{R} \cdot \exp\left(-\frac{v \cdot R}{2a}\right)\right) \quad (5)$$

$$\text{where } R = \sqrt{(x_0 - v \cdot t)^2 + y^2 + \left(z - j \cdot (k - 1) \cdot \frac{z_D}{n_q} - 2 \cdot s \cdot n\right)^2}$$

The temperature for time  $t$  and coordinates  $y, z$  is defined by laser power  $q_0$ , laser power efficiency coefficients  $\eta_{tot}$  (ref. Eq.4), and welding speed  $v$ . The material specific properties are considered by temperature independent thermal conductivity  $\lambda$  and the thermal diffusivity  $a$ . These are all determined by integration in the essential temperature range.

The heat source is in the  $x_0$  position on a sheet metal of thickness  $s$ , equivalent to the pipe geometry considered in this work. A finite number  $n_q$  of single heat sources is super-positioned over the welding depth  $z_D$ . The boundary conditions of the body are considered due to mirrored sources (sum over  $j$ ).

### 3.3 Initial and Boundary Conditions

The initial condition in this analysis is defined by the initial temperature distribution  $T(x,y,z,t_0)$ . Here, the initial temperature in the total volume corresponds to the ambient temperature (25°C). The heat flux from the outer component surface to the surrounding air is defined by an overall heat transfer coefficient  $\alpha$  considering the flux sum of the independent processes of convection  $\alpha_c$  and radiation  $\alpha_r$ . For this reason, a temperature-dependent heat transfer coefficient was implemented, according to Eq. 6:

$$\alpha = \alpha_c + \alpha_r = \alpha_c + \varepsilon \cdot \sigma \frac{(T + 273)^4 - (T_0 + 273)^4}{T - T_0} \quad (6)$$

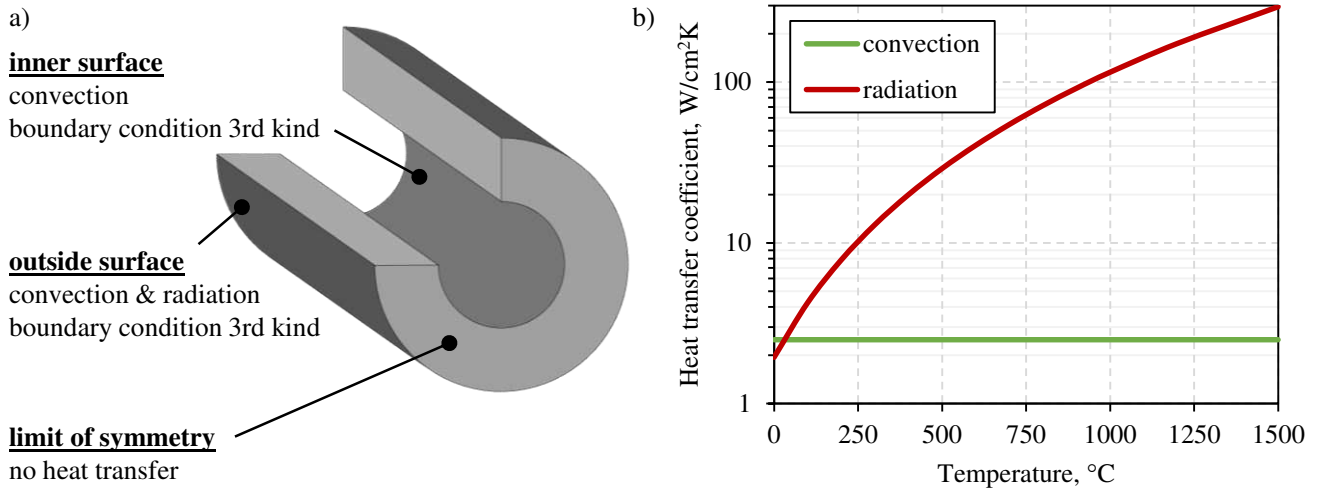


**Figure 4: Boundary conditions**

The boundary condition for the heat transfer on the inner surface was modified, considering forced convection and excluding radiative heat transfer. This assumption is based on the concept that all radiated heat is absorbed from the opposite surface, meaning that the heat sum is balanced. Moreover, almost simultaneously the temperature field becomes near axisymmetric (axis of rotation), i.e., the temperature difference on opposite surfaces is negligible. Thus, the heat transfer is modeled by a temperature-independent coefficient (pure convection) equal to  $2.5 \times 10^{-6} \text{ W m}^{-2} \text{ K}^{-1}$ . Since a semi-model is used, an adiabatic boundary is present on the symmetrical plane of the welded joint. The heat transfer due to heat conduction at the contact surface of the component with the clamping is neglected, as there is no significant heating in this region.

### 3.4 Transformation Kinetics

The material model, which defines the phase transformations, was strongly coupled with the temperature field calculation, since thermo-physical material properties vary depending on temperature and phase proportion. Diffusion controlled phase transformation (austenitization of the initial bainite), which is proven by dilatometer tests, was modelled by Leblond's [16] semi-empirical equation (Eq. 6) and applied during heating:

$$\frac{dP(T)}{dt} = \frac{P_{eq}(T) - P(T)}{\tau(T)} \quad (6)$$

With austenitization, the transformed volume fraction  $P(t)$  of a maximum fraction  $P_{eq}$ , defined for an equilibrium state to a certain temperature, is calculated by heating rate depending parameter  $\tau$ . The calibration of this parameter is accomplished by implementing transformation processes and the procedure described by [1] for the material 100Cr6. Thus, a heating rate of  $1000 \text{ K s}^{-1}$  was used to set transformation temperatures  $A_{c1}$  and  $A_{c3}$  to a fixed value of  $770^\circ\text{C}$  and  $860^\circ\text{C}$ , respectively, where  $P_{eq}$  changes from 0 to 1. The parameter  $\tau$  was then calibrated to 0.001 for different, but extremely high heating rates according to the transformation temperatures in the continuous time-temperature-austenitization diagram (TTA), as discussed by [1].

In the laser beam welding process, cooling times  $t_{8/5}$ , i.e., the time required to cool from  $800^\circ\text{C}$  to  $500^\circ\text{C}$ , less than 1 s are observed. With such rapid cooling, the austenitized phase of 100Cr6 only forms

martensite. This diffusion-free  $\gamma \rightarrow \alpha$  transformation kinetic is described by the Koistinen-Marburger [21] law (Eq. 7):

$$P_M(T) = P_A(1 - \exp[-K_M (M_S - T)]) \quad (7)$$

The martensite phase fraction  $P_M(T)$  for a temperature  $T$  results from the transformation coefficient of the Koistinen-Marburger equation  $K_M$  and the martensite start temperature  $M_S$  and depends on the primarily formed austenite phase fraction  $P_A$ . Here, austenite transforms into martensite during cooling below  $M_S$  of  $190^\circ\text{C}$  and shows no fraction of residual austenite, which is calibrated by setting  $K_M$  to 0.04.

Both metallurgical models are calibrated on the basis of heating and cooling rates, which deviate from the occurring conditions, since no data can be measured with known methods for the process conditions. Nevertheless, this simplification is not assumed to be critical because the volume of the HAZ, and thus the latent heat effect, is very small compared to the applied laser power density.

### 3.5 Material Properties

According to the described transformation kinetics, temperature, and phase dependent thermo-physical material properties were implemented. The heat input during welding leads to a local temperature increase, which varies depending on the specific enthalpy  $h$  and density  $\rho$  of the material. The resulting temperature gradient generates a directional flow depending on the thermal conductivity  $\lambda$ . Karkhin [15] uses the example of laser welding of aluminum to describe the effects of latent heat on thermal processes. He shows that considering latent heat of fusion and solidification reduces the weld width and affects the geometric course of the mushy zone (solid/liquid interface). The precision of the simulation result increases in this specific case. However, an important conclusion of his work is that simplified modeling approaches for latent heat consideration can cause significant miscalculations. In this application, latent heat was considered during austenite transformation resp. decomposition in the specific enthalpy curve when crossing transformation temperatures (section 3.4). By distinguishing  $\alpha$ - and  $\gamma$ -phase, the transformation kinetics are directly coupled to the calculation of the heat distribution. All characteristic values shown in Figure 5 have been taken from the literature [13].

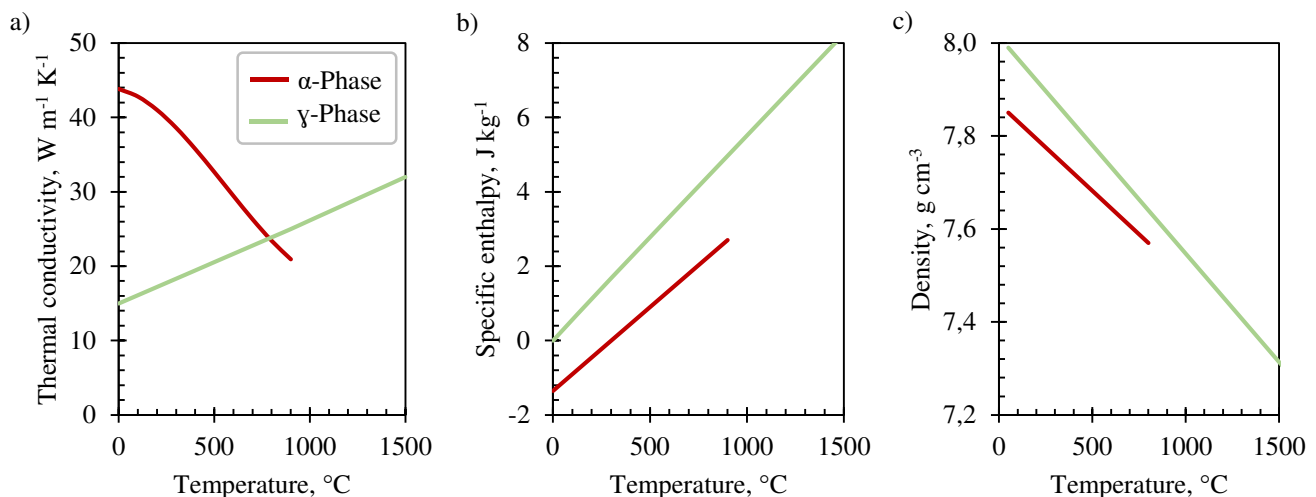


Figure 5: Thermo-physical properties of high strength steel 100Cr6

## 4. Results and Discussion

The numerical Simulation was first validated by laser beam welding experiments, where the thermocouples is attached in the area of the heat-affected zone and further away from the center of the

weld. Since the numerical simulations showed particularly high heating rates in the HAZ, the heating phase was also calculated analytically for the purpose of verification.

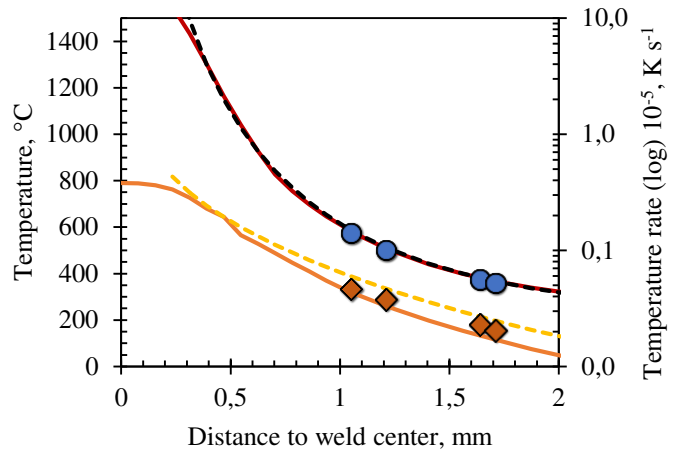
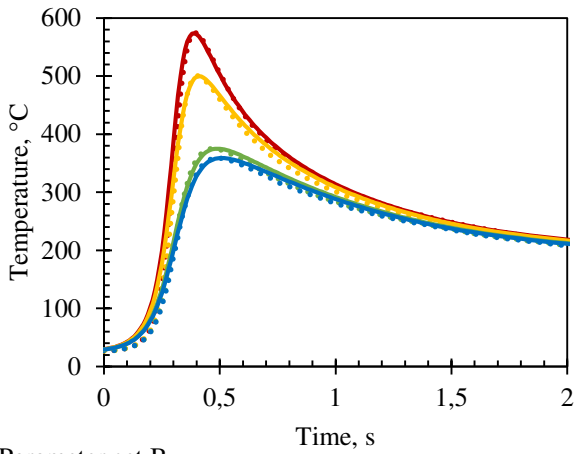
The calibration enabled the determination of the heat source parameters according to Table 2. This exhibits the greatest correlation between simulation and experimental results.

**Table 2 – Heat Source Parameters**

Parameter	Symbol	Parameter set A		Parameter set B	
		Surface source	Volume source	Surface source	Volume source
laser power	$q_0$	300 W		700 W	
Efficiency	$\eta$	5 %	73 %	14 %	53.5 %
welding speed	$v$	1 m/min		6 m/min	
angular velocity	$\omega$	4.166 rad/s		25 rad/s	
radius surface	$r_0$	1 mm	-	1 mm	-
z-Position cone limits up/below	$z_a / z_b$	-	0.25 / -1.15 mm	-	0 / -1.36 mm
radius cone up/below	$r_a / r_b$	-	0.2 / 0.35 mm	-	0.1 / 0.25 mm

All measured and calculated temperature cycles and maximum value profiles are compared with the simulation data in Figure 6.

a) Parameter set A



b) Parameter set B

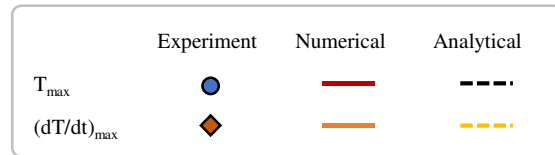
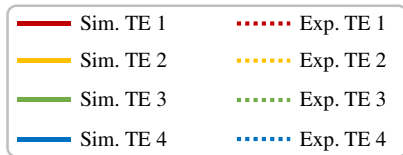
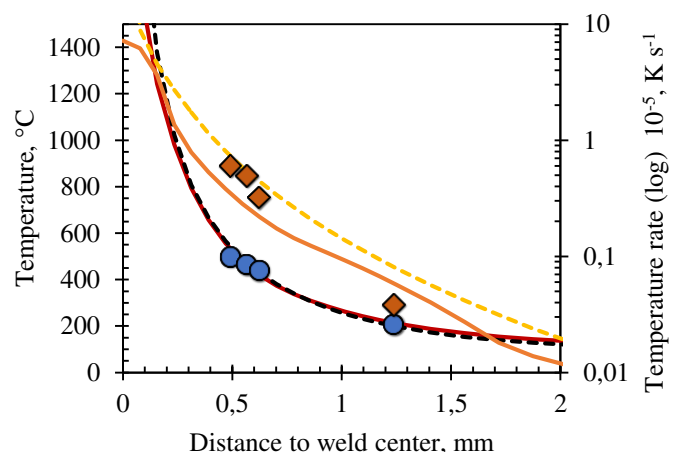
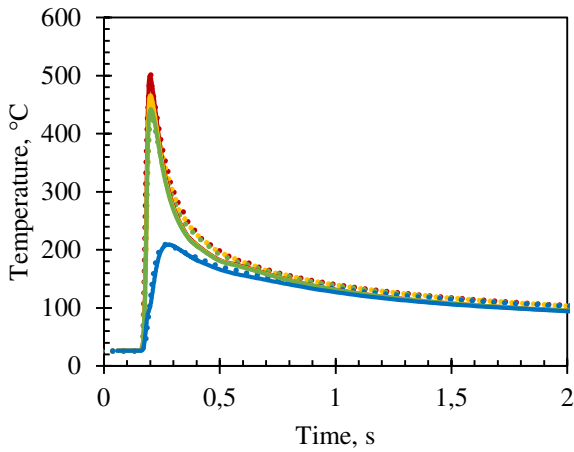


**Figure 6: Thermal cycles for the two parameter sets A (a) and B (b)**

The time-dependent temperature cycles (Fig. 6, left) of the simulation (continuous lines) consistently show an excellent agreement with the validation experiments (dashed lines) for both parameter sets. On average, the recorded difference in maximum temperature is  $8.2^{\circ}\text{C}$  for set A and  $15^{\circ}\text{C}$  for set B. Next to the temperature-time curves, the spatial distribution of the maximum temperatures and heating rates were also considered in Fig. 6 (right). In addition to the thermocouple measurements (experiments) and the numerical simulations, the analytical calculation was compared. These calculations confirmed the numerical simulations with a high degree of agreement. Along the distance (between the fusion line and 2 mm distance) to the center of the weld seam (component surface,  $180^{\circ}$  welding angle), the standard deviation in maximum temperature is 7.9 K (set A) and 16 K (set B), while the maximum heating rates are  $58\text{ K s}^{-1}$  (set A)  $1720\text{ K s}^{-1}$  (set B). Only for small weld seam distances (approx. smaller than the fusion line) does the analytical calculation becomes meaningless due to the closeness to the singularity point of the heat source equation. Furthermore, this analysis utilizes an analytical solution that is precise for the heating phase and neglects cooling.

In addition to the thermocouple measurements, the weld seam geometry is an important criterion for the quality of the thermo-physical numerical calculation. The comparison between the calculated maximum temperature distribution and the weld seam geometry, shown in cross sections, is presented in Figure 7

and Figure 8. The white areas in the calculated temperature distributions indicate the assumed molten state ( $T_{\max} > 1300^{\circ}\text{C}$ ), which can then be seen as solidified weld metal in the micrographs.

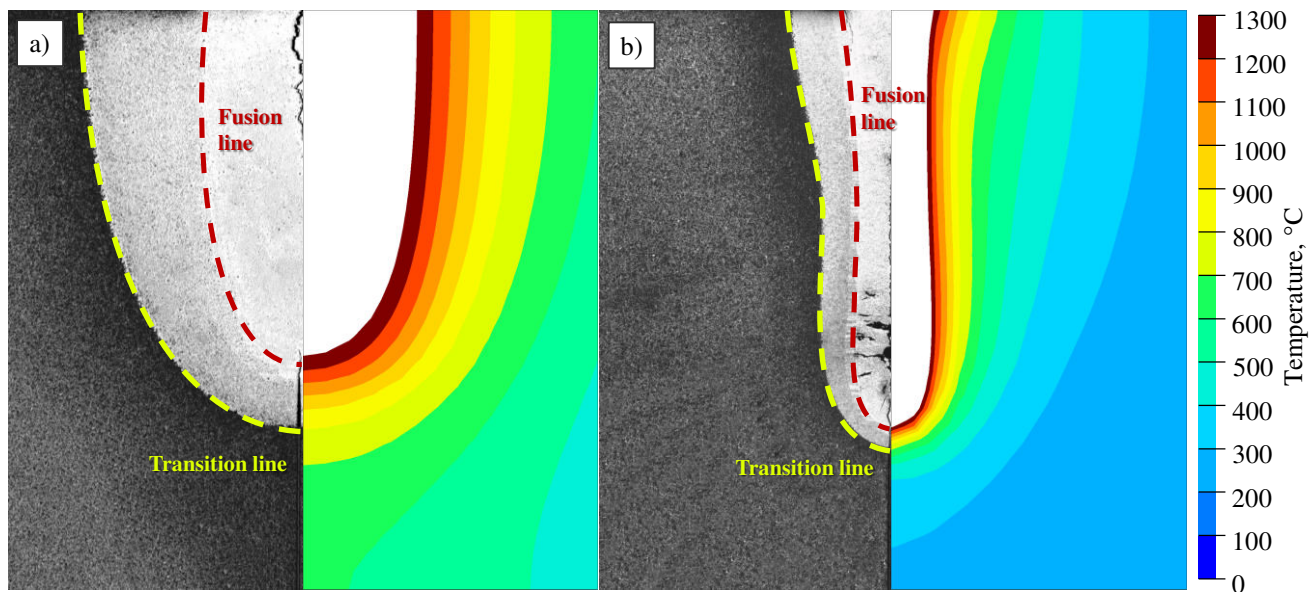


**Figure 7: Weld shape compared to the maximum temperature distribution for set A and B**

Depending on laser power and welding speed, the weld seams vary significantly in terms of geometry. Due to the much higher energy input of roughly  $18 \text{ kJ m}^{-1}$  in set A (Fig. 7 left), more heat is brought into the sample. This causes the weld seam width to be significantly larger than in set B (Fig. 7 right), which produces an energy input of about  $7 \text{ kJ m}^{-1}$ . The weld seam on the surface is wider by a factor of 2.6, whereas the weld seam depth for set B is larger by a factor of 1.2.

There are also substantial differences between the two sets of parameters in terms of local heating rates, temperature gradients, and cooling times. In general, the heating rate, in combination with the maximum temperature, offers valuable information about the transformation of the steel into the austenite phase and characterizes its homogenization. This transformation kinetic is particularly relevant for the modeling of phase proportions, as steels commonly described by TTA diagrams were often only determined for heating rates of less than  $5000 \text{ K s}^{-1}$ . Modern laser beam welding processes such as those discussed here, however, show significantly higher heating rates. In addition, the real heating rates in the relevant area of phase transformation are mostly unknown due to measurement limitations. Therefore, the local differences were considered for the welding parameters as well as for different areas of the weld seam that are technically inaccessible. To characterize the HAZ, these results are shown at the fusion line (FL) and the transition line (TL), i.e., transition between HAZ and the base metal. Hereby the  $1300^{\circ}\text{C}$  and  $860^{\circ}\text{C}$  ( $A_{c3}$ ) isotherms are respectively assumed.

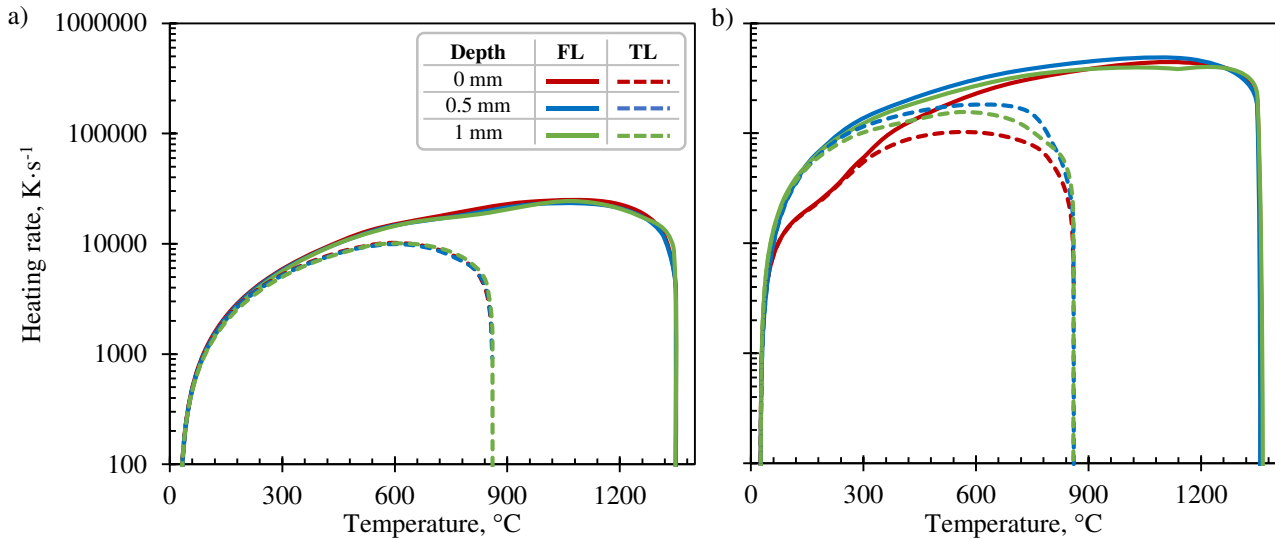


**Figure 8: Heating rates in the HAZ: (a) by set A end (b) by set B on the FL and on the TL at different weld depths**

Due to the significantly higher welding speed, the average maximum heating rate is 14.6 times higher near the transition line and 18.1 times higher on the fusion line compared to set A (Fig. 8a). In the weld seam depth direction, changes can be seen in the heating rate curve, especially for set B. Here, the maximum difference is around  $86900 \text{ K s}^{-1}$  along the fusion line. In set A, however, the greatest difference is much smaller and differs by  $1395 \text{ K s}^{-1}$  also on the fusion line. Between the fusion and transition lines, set A shows a six-fold change in heating rate, while set B decreases only in the single-digit percentage range, which is still  $6000 \text{ K s}^{-1}$ . These differences become even clearer with a distance-dependent illustration. Figure 9 shows the maximum temperature (Fig. 9a) and the maximum heating rate (Fig. 9b) as a function of the distance to the weld center for the two parameter sets.

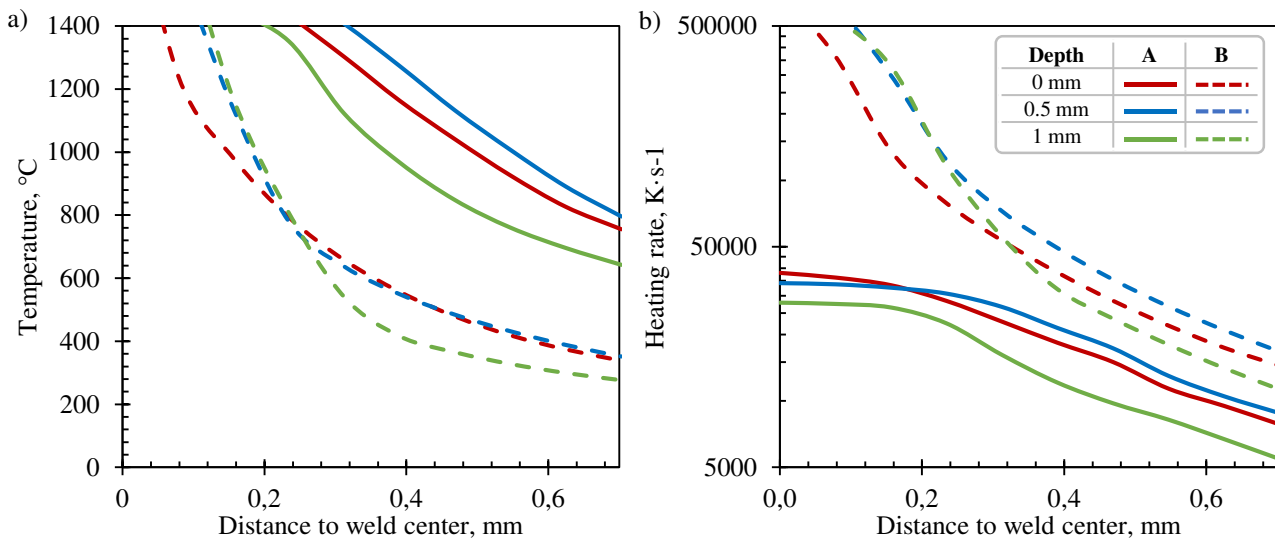


**Figure 9: Transverse distribution of maximal temperature in the HAZ for different weld depth: (a) for set A and (b) for set B**

The numerical calculations show characteristic differences in maximum temperature and heating rate distribution. While the maximum temperature for set A rises quite evenly towards the fusion zone, set B exhibits an increase in the maximum temperature rise, especially at depth, before exceeding  $A_{c3}$  at approx.  $0.258 \text{ mm}$  distance to the weld center. In the HAZ of set A, the maximum temperature distribution graduates by an average of  $1200 \text{ K mm}^{-1}$ , while set B shows a 60% higher increase of around  $1920 \text{ K mm}^{-1}$ .

<sup>1</sup>. The importance of exact installation and measurement of thermocouples becomes clear in a case such as this. Short distances can already make a profound difference to the measured maximum temperature. The example of set B underlines this in showing that the temperature gradients are extremely different. The calculated maximum heating rate distribution shows similar characteristics. Figure 9b verifies that the previously described differences in the heating rates extend over the entire HAZ under consideration and that both parameter sets show values greater than  $5000 \text{ K s}^{-1}$ . While the spatial change of maximum heating rate over the sub-zones of HAZ graduates by an average rate of  $32.5 \times 10^3 \text{ K s}^{-1} \text{ mm}^{-1}$  for set A, set B shows a 23.6-times higher derivation of approximately  $769 \times 10^3 \text{ K s}^{-1} \text{ mm}^{-1}$ .

The microstructural changes in the weld zone are also greatly dependent on the cooling rates. For fast cooling times, which are often characterized by the time differences between  $800^\circ\text{C}$  and  $500^\circ\text{C}$  ( $t_{8/5}$  time), high-strength steels usually show hardening due to the formation of martensite. With cooling times of less than one second, martensite formation can generally be assumed. The temperature cycles also show very different cooling rates (Fig. 10) for the respective parameter sets, but both are well below the cooling time  $t_{8/5}$  of one second.

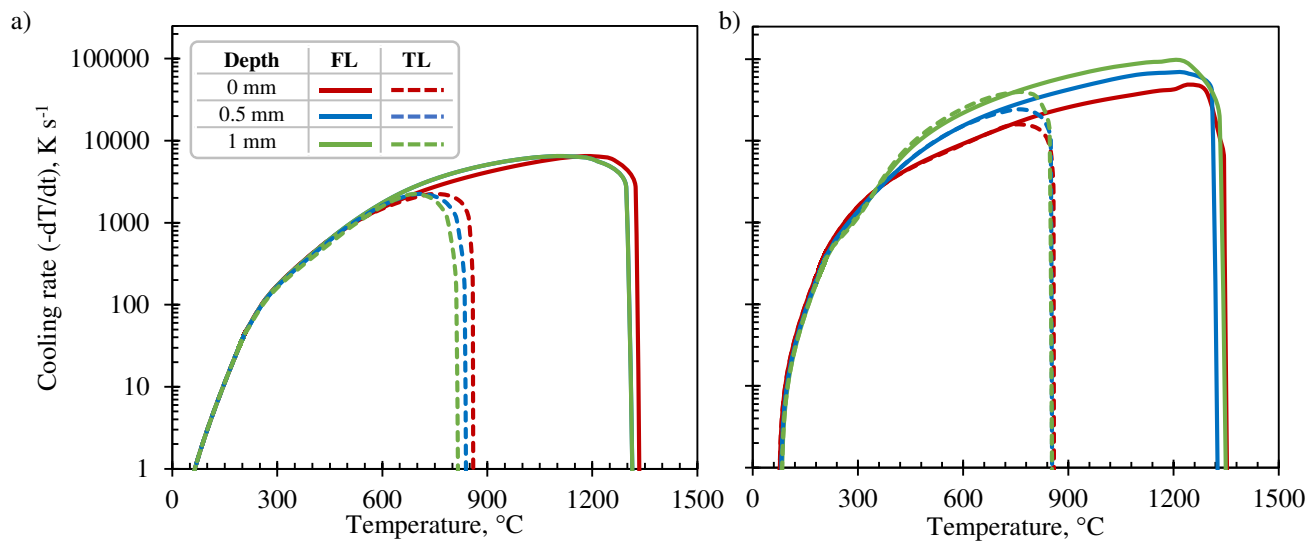


**Figure 10: Absolute values of cooling rates in the HAZ ( $-dT/dt$ ): (a) for set A and (b) for set B, on to the FL and TL, in transverse direction and for different weld depths.**

Near the fusion line they reach maximum values of roughly  $-6480 \text{ K s}^{-1}$  (set A) and  $-92360 \text{ K s}^{-1}$  (set B). The values are  $-2250 \text{ K s}^{-1}$  (set A) and  $-39000 \text{ K s}^{-1}$  (set B), near the transition line. In the range between  $800^\circ\text{C}$  and  $500^\circ\text{C}$ , the cooling rates show an average of about  $-2023 \text{ K s}^{-1}$  ( $0.15 \text{ s } t_{8/5}$ -time, set A) and  $-17590 \text{ K s}^{-1}$  ( $0.017 \text{ s } t_{8/5}$ -time, set B). Near the transition line, the values are  $-1350 \text{ K s}^{-1}$  ( $0.22 \text{ s } t_{8/5}$ -time, set A) and  $-12200 \text{ K s}^{-1}$  ( $0.025 \text{ s } t_{8/5}$ -time, set B).

## 5. Conclusion

In this study, a three-dimensional numerical model was developed and applied for the calculation of thermal cycles, as well as weld and HAZ shapes during butt-joint laser beam welding of high strength steel 100Cr6 without filler material. Therefore, a heat conduction model was applied, which assumes infinity energy propagation velocity. The main conclusions of this analysis are as follows:

1. The objective of the temperature field study is the laser beam welding of circular welds from high strength steel (different parameter sets), both qualified for cold crack testing. Special attention was paid to the distribution of maximum temperatures and temperature rates.

2. The temperature field was simulated using a strong coupled model, considering the heat distribution and temperature and metallurgical phase dependent material properties. The simulation results were validated by comparing experimental data, and the heating phase was also confirmed via analytical calculation.
3. The heat source was modeled by a combination of two normal distributed heat source models: a conical heat source model and a surface heat source model. This combined heat source is suitable for both studied welding process variations. The numerical calibration results show that decreasing the laser beam power also decreases the contribution of surface thermal flux. At relatively low power, it practically vanishes.
4. By changing the energy per unit length by a factor of 0.4 and the welding speed by a factor of 6, the weld seam width can be reduced by a factor of 2.6, while the welding depth increases by a factor of 1.2. The increase in averaged slope of maximum temperature distribution curves is two to four times higher near the fusion line compared to transition line. In both sets, the temperature field is extremely narrow, and the parameters of the welding thermal cycle drop in a transverse direction in range of a few tenths of a millimeter.
5. The heating rates in the HAZ (e.g.,  $5 \times 10^3$  to  $5 \times 10^4$  K s<sup>-1</sup>) are significantly above the value ranges typically addressed by TTA diagrams. Similarly, the cooling times are significantly less than one second (e.g.,  $10^{-1}$  to  $10^{-2}$  s) for both parameter sets, which are also outside the common range considered in CCT diagrams. Despite the slight influence on the calculation result due to the small volume involved, this relationship requires further research into new, adapted investigation methods.

## **Acknowledgment**

The authors thank the Federal Ministry of Education and Research (BMBF) for financial support as part of the joint project “SimCoLas - Simulation Controlled Laserwelding”. (Funding code 13N13832)

## **Declarations**

### a. Funding

The work was financially supported by the Federal Ministry of Education and Research (BMBF) as part of the joint project “SimCoLas - Simulation Controlled Laserwelding” in collaboration with Robert Bosch GmbH, Föhrenbach Positioniersysteme GmbH, Anton Häring KG, Volkswagen AG and Bundesanstalt für Materialforschung und -prüfung (BAM). (Funding code 13N13832)

The authors declare that no additional funds, grants, or other support were received during the preparation of this manuscript.

### b. Competing Interests

The authors have no relevant financial or non-financial interests to disclose.

### c. Availability of data and material

Not applicable

### d. Code availability

Not applicable

### e. Ethics approval

The authors believe that neither the manuscript nor the study violates any rules of good scientific practice or ethical standards.

f. Consent to participate

Not applicable

g. Consent for publication

Not applicable

h. Author Contributions

All authors contributed to the study conception and design. Material preparation, data collection and analysis were performed by Eric Wasilewski with support from Nikolay Doynov and Ralf Ossenbrink. The first draft of the manuscript was written by Eric Wasilewski, reviewed by Nikolay Doynov and Ralf Ossenbrink. Vesselin Michailov is the principle investigator. All authors read and approved the final manuscript.

## References

- [1] O. Dreibati, Physical welding simulation of the cold crack susceptibility. Aachen: Shaker, 2014.
- [2] D. Radaj, Heat Effects of Welding: Temperature Field, Residual Stress, Distortion. Berlin, Heidelberg: Springer Berlin Heidelberg, (1992).
- [3] D. Radaj, Schweißprozeßsimulation: Grundlagen und Anwendungen. Düsseldorf: Verl. für Schweißen und verwandte Verfahren DVS-Verl., (1999).
- [4] N. N. Rykalin, Laser and electron beam material processing: Handbook. Moscow: Mir Publishers, (1988).
- [5] J. Goldak, M. Bibby, J. Moore, R. House und B. Patel, „Computer modeling of heat flow in welds“, MTB, Jg. 17, Nr. 3, (1986), S. 587–600.
- [6] A. Artinov, M. Bachmann und M. Rethmeier, „Equivalent heat source approach in a 3D transient heat transfer simulation of full-penetration high power laser beam welding of thick metal plates“, International Journal of Heat and Mass Transfer, Jg. 122, Nr. 2, (2018), S. 1003–1013.
- [7] A. Evdokimov, K. Springer, N. Doynov, R. Ossenbrink und V. Michailov, „Heat source model for laser beam welding of steel-aluminum lap joints“, The International Journal of Advanced Manufacturing Technology, Jg. 93, 1-4, (2017), S. 709–716.
- [8] G. X. Xu, C. S. Wu, G. L. Qin, X. Y. Wang und S. Y. Lin, „Adaptive volumetric heat source models for laser beam and laser + pulsed GMAW hybrid welding processes“, The International Journal of Advanced Manufacturing Technology, Jg. 57, Nr. 1, (2011), S. 245–255.
- [9] J. Rahman Chukkan, M. Vasudevan, S. Muthukumaran, R. Ravi Kumar und N. Chandrasekhar, „Simulation of laser butt welding of AISI 316L stainless steel sheet using various heat sources and experimental validation“, Journal of Materials Processing Technology, Jg. 219, (2015), S. 48–59.
- [10] J. B. Leblond und J. Devaux, „A new kinetic model for anisothermal metallurgical transformations in steels including effect of austenite grain size“, Acta Metallurgica, Jg. 32, Nr. 1, (1984), S. 137–146.
- [11] D. P. Koistinen und R. E. Marburger, „A general equation prescribing the extent of the austenite-martensite transformation in pure iron-carbon alloys and plain carbon steels“, Acta Metallurgica, Jg. 7, Nr. 1, (1959), S. 59–60.

- [12] H. Zhang, Y. Wang, T. Han, L. Bao, Q. Wu und S. Gu, „Numerical and experimental investigation of the formation mechanism and the distribution of the welding residual stress induced by the hybrid laser arc welding of AH36 steel in a butt joint configuration“, *Journal of Manufacturing Processes*, Jg. 51, (2020), S. 95–108.
- [13] F. Schweizer, „Simulation von Laserschweißprozessen zur Bewertung der wasserstoffbeeinflussten Kaltrissneigung hochfester Stähle“. Dissertation, KIT-Bibliothek, Karlsruhe, 2016.
- [14] M. Matic, „Laserstrahlschweißen hochfester Werkstoffe an rotationssymmetrischen Bauteilen“. Hochschulschrift, Dresden, (2011).
- [15] V. A. Karkhin et al., „Effects of latent heat of fusion on thermal processes in laser welding of aluminium alloys“, *Science and Technology of Welding and Joining*, Jg. 10, Nr. 5, (2005), S. 597–603.